



**AIAA-2002-4409**

**Supersonic Aerodynamic  
Characteristics of Proposed Mars '07  
Smart Lander Configurations**

Kelly J. Murphy, Thomas J. Horvath,  
Gary E. Erickson  
*NASA Langley Research Center  
Hampton, VA 23681*

Joseph M. Green  
*Mississippi State University  
Mississippi State, MS 39762*

**AIAA Atmospheric Flight Mechanics  
Conference and Exhibit  
5-8 August 2002/ Monterey, California**

For permission to copy or republish, contact the American Institute of Aeronautics and Astronautics  
370 L'Enfant Promenade, S.W., Washington, D.C. 20024



# Supersonic Aerodynamic Characteristics of Proposed Mars '07 Smart Lander Configurations

Kelly J. Murphy\*, Thomas J. Horvath\*†, Gary E. Erickson†  
NASA Langley Research Center, Hampton, VA 23681

Joseph M. Green‡  
Mississippi State University, Mississippi State, MS 39762

Supersonic aerodynamic data were obtained for proposed Mars '07 Smart Lander configurations in NASA Langley Research Center's Unitary Plan Wind Tunnel. The primary objective of this test program was to assess the supersonic aerodynamic characteristics of the baseline Smart Lander configuration with and without fixed shelf/tab control surfaces. Data were obtained over a Mach number range of 2.3 to 4.5, at a free stream Reynolds Number of  $1 \times 10^6$  based on body diameter. All configurations were run at angles of attack from -5 to 20 degrees and angles of sideslip of -5 to 5 degrees. These results were complemented with computational fluid dynamic (CFD) predictions to enhance the understanding of experimentally observed aerodynamic trends. Inviscid and viscous full model CFD solutions compared well with experimental results for the baseline and 3 shelf/tab configurations. Over the range tested, Mach number effects were shown to be small on vehicle aerodynamic characteristics. Based on the results from 3 different shelf/tab configurations, a fixed control surface appears to be a feasible concept for meeting aerodynamic performance metrics necessary to satisfy mission requirements.

## Nomenclature

$C_A$	axial-force coefficient
$C_D$	drag-force coefficient
$C_L$	lift-force coefficient
$C_{L\alpha}$	lift-force curve slope
$C_l$	rolling-moment coefficient
$C_{l\beta}$	rolling-moment beta derivative, $dC_l/d\beta$
$C_m$	pitching-moment coefficient
$C_{m\alpha}$	pitching-moment alpha derivative, $dC_m/d\alpha$
$C_n$	yawing-moment coefficient
$C_{n\beta}$	yawing-moment beta derivative, $dC_n/d\beta$
$C_N$	normal-force coefficient
$C_{N\alpha}$	normal-force alpha derivative, $dC_N/d\alpha$
$C_Y$	side-force coefficient
$L_{ref}$	longitudinal reference length
$M$	Mach number
$p_\infty$	static pressure of free stream, psia
$p_t$	tunnel stagnation pressure, psia
$q_\infty$	free stream dynamic pressure, psia
$Re_\infty$	free stream unit Reynolds number/ft
$S_{ref}$	reference area
$S_{Ames}$	"Ames" tab reference area
$S_{Canted}$	"Canted" tab reference area
$S_{Shelf}$	"Shelf" reference area
$T_\infty$	static temperature of free stream, °R
$T_t$	tunnel stagnation temperature, °R
$\alpha$	angle of attack, deg
$\beta$	angle of sideslip, deg

## Introduction

As part of NASA's on-going Mars Exploration Program, several planned missions include sample return requirements. These future missions will require a highly precise entry through the Martian atmosphere and a "smart" landing with the ability to detect and avoid hazards on the planet's surface. A key component to enabling these highly accurate trajectories and precise landings is reduction of uncertainties in the aerodynamic characteristics of the vehicle's aeroshell. The Mars '07 Smart Lander program was established to land a vehicle on the Martian surface with the dual goals of furthering basic scientific research on Mars as well demonstrating a host of "smart" technologies needed for a Mars Sample Return mission. Smart Lander technology goals include demonstration of a precision landing within a  $\pm 5$ -kilometer footprint and a 100-meter site redesignation capability for hazard avoidance, enabling surface mobility of a rover to successfully navigate from the landing site to a pre-determined target location.<sup>1</sup>

Both low-L/D and mid-L/D aeroshell shapes were initially considered among the numerous '07 Lander trade studies,<sup>2</sup> but the focus was eventually turned to a low-L/D shape with Pathfinder/Viking heritage. The Mars '07 Lander baseline aeroshell is a 4.05-meter diameter spherically blunted 70-degree cone with a biconic backshell (Fig. 1). The large cone half-angle is required to produce the necessary drag to decelerate the Lander's entry mass (approximately 2300 kg) at sufficiently high altitudes to permit parachute deployments in both the supersonic and subsonic flight regimes. To provide sufficient control authority and the necessary cross range capability, the configuration

\*Aerospace Technologist, Aerothermodynamics Branch, Aerodynamics, Aerothermodynamics and Acoustic Competency

† Aerospace Technologist, Research Facilities Branch, Aerodynamics, Aerothermodynamics and Acoustic Competency

‡ Aerospace Engineering Cooperative Education Student, Mississippi State University.

† Member AIAA

must achieve sufficient trimmed L/D, which is generally obtained via geometric asymmetry and/or offset of the vehicle center of gravity (c.g.). Minimizing radial c.g. offsets can reduce ballast requirements, provide internal packaging benefits, and thus yield corresponding optimization in weight and performance. One proposed solution to attaining higher L/D values with less mass penalty is a fixed control surface, a shelf or tab, attached in the corner or shoulder region and of a suitable geometry to satisfy aerodynamic requirements.<sup>1,2</sup>

Initial design goals for the '07 Smart Lander aeroshell with a fixed shelf/tab control surface include a trimmed L/D of 0.25 with no radial center of gravity offset. Naturally it is desired to minimize shelf/tab mass to minimize corresponding ballast mass and therefore increase payload capability. An additional design constraint is that a fixed shelf/tab configuration must fit within the maximum payload diameter (approximately 4.5m) of the Delta IV launch vehicle's fairing. Current trajectories show supersonic parachute deployment at a nominal Mach number of 2.2. Thus, obtaining supersonic aerodynamic wind tunnel data became a priority to reduce uncertainties in initial design/trade studies for the '07 Lander. This experimental data, in conjunction with ballistic range data, supersonic and hypersonic CFD predictions, and mechanical design/package requirements, will be used to optimize a proposed control surface design for the '07 Smart Lander.

### **Objectives**

To provide vehicle designers with necessary supersonic aerodynamic data, a sub-scale model of a proposed Smart Lander Configuration was designed, fabricated, and tested in Leg II of the Unitary Plan Wind Tunnels at the NASA Langley Research Center. The test program described in this paper was designed to satisfy two primary objectives:

**(1) Provide aerodynamic data in the supersonic speed regime to establish the stability and performance characteristics of the proposed baseline Mars '07 Smart Lander and to validate CFD predictions; (2) Provide data to assess aerodynamic characteristics of three shelf/tab configurations.**

To accomplish the first objective, a 0.0376-scale aluminum force and moment Smart Lander model was fabricated for testing in the UPWT. An extensive matrix of 6-component force and moment data was taken on the model using a strain-gage force and moment balance. Over 80 runs were made in the UPWT over a range of supersonic Mach numbers to characterize baseline vehicle stability and control and performance characteristics at relevant angles of attack and sideslip. A number of these runs were part of an extensive data quality program to ensure the smallest possible data uncertainties. To address this second objective, three different shelf/tab configurations were

fabricated at LaRC for testing in the UPWT. Over 60 runs were conducted to assess the control effectiveness and performance characteristics of these control surfaces.

### **Experimental Program**

#### **Model Description**

All experimental aerodynamic data presented in this report were obtained with a 0.0376-scale metallic force-and-moment model designed and fabricated in-house at NASA Langley. The model diameter was 6 inches, and the nominal reference areas and lengths used to calculate aerodynamic coefficient data for the full-scale vehicle and the 0.00376-scale model are presented in Table 1.

All model components were fabricated from aluminum and included 3 removable shelf/tab configurations. Schematic drawings of these control surfaces are presented in Fig. 2. The "Ames Recreated" (which will be referred to as "Ames") surface is a somewhat square-shaped tab, located at maximum vehicle diameter, with a full-scale area of 9.372 ft<sup>2</sup>. This tab shape was one generated in initial parametric studies. It was retained for these tests for comparisons to Ames ballistic range data as well as comparisons to the blended canted tab and blended shelf configurations, which are refined versions of earlier designs. The blended canted tab (referred to as "canted") has a full-scale area 5.659 ft<sup>2</sup>. It is located at the maximum diameter of the vehicle and is angled at 80 degrees to the axis of symmetry of the 70-degree sphere cone heatshield. The blended shelf (referred to as "shelf") is a continuation of the windward aeroshell angled at the same 70-degree slant to the axis of symmetry. The shelf full-scale area is 7.628 ft<sup>2</sup>. Control surface areas corresponding to both full-scale and a 0.0376 model-scale are summarized in Table 2.

A non-metric aluminum balance sleeve was fabricated to shield the portion of the force balance that protruded from the model from the tunnel flow to minimize balance heating and loading due to flow impingement. A photograph showing design of this sleeve is shown in Fig 3.

The outer mold lines of the aerodynamic model were extensively checked against Lander geometry files by Langley's Surface Verification Laboratory. The x,y,z-location of numerous surface contour points were measured using both global and discrete point techniques to characterize surface coordinate fidelity: All of the measured contour points were within  $\pm 0.005$  in. of configuration outer-mold-line definition. These surface measurements were also used to precisely determine balance bore alignment and balance electrical center (i.e. c.g) location for accurate calculation of model attitude and moment transfer distances.

#### **Facility Description**

*Unitary Plan Wind Tunnel-Leg II:* The UPWT is a closed-circuit, continuous-running, pressure

tunnel with two test sections that are nominally 4 ft by 4 ft in cross section and seven ft long. The stagnation pressure,  $p_t$ , can be varied up to a maximum of approximately 50 psia in Test Section I and approximately 100 psia in Test Section II. The nozzle throat-to-test-section area ratio is varied by a lower asymmetric sliding nozzle block that provides continuous variation of the Mach number. The Mach number range is nominally 1.5 to 2.86 in Test Section I and 2.3 to 4.63 in Test Section II. Tunnel stagnation temperatures,  $T_t$ , are typically 125 °F and 150 °F for each test section, respectively. Reynolds numbers from 1.0 to 5.0 million per foot are possible. The basic model support mechanism is a horizontal wall-mounted strut that is capable of forward and aft travel of over 3 ft in the streamwise direction. A main sting support attached to the strut can transverse laterally  $\pm 20$  in and can provide a yaw capability of  $\pm 12^\circ$ . Forward of the main sting support is the angle-of-attack mechanism that provides pitch motion from  $-15^\circ$  to  $+30^\circ$ . A roll mechanism can be installed ahead of the pitch mechanism to provide continuous roll motion over a  $310^\circ$  range. The history and test capabilities of the UPWT are discussed in Ref. 3.

#### Instrumentation and Data Uncertainty

Three aerodynamic forces and three aerodynamic moments were measured using the 6-component strain gage balance designated as the Langley 2008. Wind-off balance readings were monitored before and after each run, and balance components were monitored during the tunnel run for drift caused by thermal gradients across the balance gages. Due to model and balance geometries, a significant portion of the force balance extended beyond the model base (Fig. 3). Thus, despite the presence of the balance sleeve to shield the model from the flow, relatively large temperature gradients were recorded across the length of the balance. For this reason runs were reduced throughout the test program using "hot-zeros," i.e., wind-off balance zero readings taken before and after each run (rather than only at the beginning of each shift) to capture slight zero shifts due to temperature gradients. This practice was shown to significantly reduce temperature effects on aerodynamic data and produce repeatabilities within quoted balance accuracies (further explained below). The balance uncertainties for representative flow conditions are shown in Table 3. Static pressure measurements were made at the base of the model within the sting shroud using an offboard electronically scanned pressure (ESP) module.

To verify that data were repeating within quoted balance accuracies, multiple repeat runs were obtained throughout the test program for the baseline configuration at Mach 2.3. Mach 2.3 produced the most severe (highest pressure and temperature) test conditions, and thus it was presumed that these data would be a worst case estimate on repeatability. "Residual" plots of six-component body-axis coefficient data were calculated by subtracting the coefficient value

in a given run, interpolated to a nominal angle of attack, from average values computed at those same nominal angles. The variation was compared to quoted accuracies for all six components based on the  $\pm 95\%$  confidence level from balance calibration reports. All residual data were shown to be bounded well by these quoted balance accuracies through the angle of attack range.

It should be noted that the aforementioned balance accuracies represent only the uncertainties associated with the balance itself. This would be a measure of the overall uncertainty on the wind tunnel measurements only in the absence of all other variations. An extensive test program involving large numbers of repeat runs on all configurations at all test conditions over multiple test entries would be required to obtain rigorous uncertainty values. In the screening and development phase of a configuration, this level of testing is simply not feasible. Thus a factor of 3 times the quoted balance uncertainties has been recommended as a conservative and physically reasonable estimate of overall uncertainties for the data generated in these tests to account for all other sources of random variation.<sup>4</sup>

#### Test Parameters

The test matrix for all of the supersonic data obtained in this test entry is shown in Table 4. The model angle of attack ranged from  $-5$  to  $20$  degrees, and the model angle of sideslip ranged from  $-5$  to  $5$  degrees. Data were obtained at Mach 2.3, 2.7, 3.5, and 4.5 for the baseline, the Ames, the canted, and the shelf configurations.

#### Computational Methods

CFD calculations were performed for selected configurations over a range of angle of attack and Mach number to complement the experimental database and to provide data at flight conditions. An inviscid Euler code, FELISA, and a finite-volume, Navier-Stokes solver, USM-3D, were used to obtain aerodynamic data.

The FELISA<sup>5</sup> (Finite Element Langley Imperial College Swansea Ames) software package combines a series of codes that generate unstructured tetrahedral grids over complex three-dimensional geometries and solve the steady three-dimensional Euler equations on these grids. Unstructured mesh methods are ideally suited for rapid analysis, as was required for early parametric assessment of control surface effectiveness, because they have the capability to greatly reduce the time associated with grid generation on complex configurations as compared to traditional block-structured methods. The mesh generator within the FELISA package carries out the discretization of the three-dimensional computational domain into tetrahedra. The FELISA unstructured mesh flow solver uses an edge-based finite-volume formulation. Fluxes are computed using a flux vector splitting scheme that is capable of representing constant enthalpy solutions.

USM3D<sup>6</sup> is a three-dimensional, cell-centered, finite volume Euler and Navier-Stokes flow solver. Computations are done on unstructured meshes using the tetrahedral grid generator VGRIDns. Inviscid flux quantities are computed across each cell face using Roe's flux-difference splitting. Spatial discretization is accomplished using an analytical formulation for computing solution gradients within tetrahedral cells. The solution is advanced to a steady state condition by an implicit backward Euler time-stepping scheme.

Computational results were obtained for all four configurations at Mach numbers of 2.3, 2.7, 3.5, and 4.5. Inviscid calculations were performed on the forebody alone as well as the full wind tunnel model. Viscous solutions were obtained for the wind tunnel model with a turbulent boundary layer. A subset of this data will be shown and compared with the experimental data in subsequent sections. In Ref. 7 Prabhu presents a thorough discussion of inviscid methods, models, and data. Viscous methods and results are presented in Ref. 8.

## **Results and Discussion**

### **Preface**

In a fast-paced study to satisfy a request for supersonic experimental aerodynamic data on proposed Smart Lander configurations, over 140 runs were obtained in Langley's UPWT (Fig. 4). The most relevant data will be presented in the sections that follow. The standard aerodynamic coordinate system is used for all measurements and analysis (Fig. 5). All moment data is reduced about the vehicle nose (x,y,z-location (0,0,0) shown in Fig. 5). Longitudinal data are of primary interest and are presented in coefficient form for both body axes,  $C_N$ ,  $C_A$ , and  $C_m$ , and stability axes  $C_L$ ,  $C_D$ , and  $L/D$ .

### **Mach Number Effects**

All configurations were run at sideslip to obtain lateral-directional data, and these data showed little variation with Mach number. Data showed all configurations (baseline and asymmetric) to be essentially neutrally stable in roll ( $C_{l\beta} \approx 0$ ) and stable in yaw ( $C_{n\beta} \approx 0.002$ ).

**Baseline Configuration:** Longitudinal aerodynamic coefficients are shown versus angle of attack in Figs. 6(a)-6(f). Data is presented for four Mach numbers from 2.3 to 4.5 at a free stream Reynolds number based on model maximum diameter of  $1 \times 10^6$ . Axial force is presented in coefficient form in Fig. 6(a). All  $C_A$  data presented in this report are uncorrected for sting/base interference effects, which are expected to be small based on the low pressures ( $C_p$  values were on the order of  $-1/M_\infty^2$ , as seen in earlier studies on the Viking configuration in UPWT) measured within the sting shroud. Data at all Mach numbers show a maximum axial force at zero degrees angle of attack, as expected, with nearly symmetric trends (within balance accuracy limitations) between  $\pm 5$

degrees angle of attack. Axial force decreases rapidly with increasing (or decreasing, as one could infer from symmetry considerations) angle of attack. Two distinct groupings of axial force trends are noticed. Data at Mach 2.3 and 2.7 lie in an upper band with a maximum  $C_A$  of approximately 1.54, while data at Mach 3.5 and 4.5 lie in a lower band with a maximum of just over 1.51. Inviscid calculations on the forebody only<sup>7</sup> show curves of similar shape but with nearly equally spaced increments in  $C_A$  with a corresponding change in Mach number. One can look to viscous effects, aftbody effects, or some combination of both to explain the small but non-linear Mach effects seen for baseline axial force measurements. Due to test time limitations, no diagnostics were performed to investigate the state of the boundary layer or aftbody flow separation/reattachment patterns on the experimental model. Both would be recommended for further study to better understand the aforementioned axial force trends. As expected for a blunt body at low to moderate angles of attack, the coefficient of drag,  $C_D$ , shown in Fig. 6(e), mirrors the behavior of  $C_A$  for all angles of attack and Mach numbers tested.

Fig. 6(b) shows normal force as a function of angle of attack for all supersonic Mach numbers tested. Magnitudes of  $C_N$  are very small compared with those of  $C_A$ . Data for all Mach numbers show near zero normal force at  $\alpha=0^\circ$ , as expected for a symmetric configuration. However, the slope of the normal force curve at  $\alpha=0^\circ$  is negative for  $M=2.3$  and  $M=2.5$ . At  $M=3.5$  and  $M=4.5$ ,  $C_{N\alpha}$  is positive in and around  $\alpha=0^\circ$  and only slightly smaller in magnitude than at larger angles of attack. For the two lowest Mach numbers, a negative  $C_{N\alpha}$  at  $\alpha=0^\circ$  leads to a negative normal force for small (less than approximately  $2^\circ$ ) angles of attack. While somewhat counter-intuitive, this trend was observed for UPWT data on the Viking aeroshell<sup>9</sup> at low supersonic Mach numbers. Inviscid forebody CFD results show no evidence of these trends for any Mach number while viscous solutions<sup>8</sup> (to be presented and discussed in the section that follows), shows slightly negative values of  $C_{N\alpha}$  for  $0^\circ < \alpha < 5^\circ$ . This again highlights likely effects of viscosity and aftbody geometry on configuration aerodynamics. While interesting from a fluid dynamics perspective, the magnitudes of  $C_N$  are so small as not to show any significant effects on lift, drag, and pitching moment characteristics as seen in Figs. 6(c)-6(f).

Pitching moment for the baseline configuration, shown in Fig. 6(c), is stable and nearly linear for all angles of attack and Mach numbers.  $C_m$  at  $\alpha=0^\circ$  is nominally zero and  $C_{m\alpha}$  is approximately -0.0024 for all data. Any variations in  $C_m$  and  $C_{m\alpha}$  with Mach number are over an order of magnitude smaller than the pitching moment increments of any control surface tested (to be shown in later sections of this paper). Figs 6d and 6f show lift coefficient,  $C_L$ , and lift-to-drag ratio,  $L/D$ , also to be nearly linear with angle of attack and independent of Mach number variation for most of the data set. Slight Mach number effects are seen in  $C_L$  for  $\alpha > 10^\circ$ , a direct result of the previous Mach number

effects for  $C_A$ . Lift is zero at  $\alpha=0^\circ$  for all configurations. For  $\alpha<10^\circ$ ,  $C_{L\alpha}$  is approximately  $-0.024$  and for  $\alpha>10^\circ$   $C_{L\alpha}$  is approximately  $-0.016$ . Fig. 6(f) shows that the baseline achieves its target magnitude of  $L/D=0.25$  at  $\alpha\approx 16^\circ$ .

**Asymmetric Configurations:** The detailed discussion in the preceding section on the effects of angle of attack and Mach number on the baseline configuration is equally applicable to all three asymmetric configurations. The coefficient trends are similar for all configurations but differ in magnitude due to the various fixed control surfaces. The increases in axial force due to increased planform area have a prominent effect on  $C_L$ ,  $C_D$ , but a lesser effect on  $L/D$ . The asymmetry in each configuration yields a non-zero trim angle, as desired. Comparison of the magnitude of the aforementioned changes in lift, drag, and pitching moment for the asymmetric configurations will be presented in a subsequent section.

### Comparison with Computational Results

Figures 7(a)-7(f) show comparison of the previously discussed experimental results for the baseline configuration with both inviscid and viscous computational data at Mach 2.3. Inviscid calculations were performed initially for the forebody only to quickly generate solutions on multiple configurations for trade study requirements. To evaluate the contributions of the aftbody, additional inviscid computations were performed on the complete wind tunnel configuration (full model with a support sting). Both sets of inviscid axial force data are shown in Fig. 7(a). Although trends are similar, inviscid forebody-alone solutions fall well below measured values of axial force across the entire angle of attack range. Corresponding inviscid solutions on the complete wind tunnel model show very good agreement with experimentally obtained  $C_A$  data for all angles of attack. The fully viscous solutions from USM-3D also show excellent axial force agreement with experimental data, especially at the highest angles of attack.

Figure 7(b) shows  $C_N$  versus alpha for the baseline configuration with accompanying inviscid and viscous calculations. Neither forebody nor full-model inviscid solutions show evidence of the non-linear trends for normal force observed around  $\alpha=0^\circ$ . As mentioned previously, the viscous solutions show a change in sign for  $C_{N\alpha}$  at low angles of attack, and thus a more detailed analysis of viscous computations may provide some insight into experimentally observed trends.  $C_{N\alpha}$  exhibits a noticeable increase for  $\alpha>15^\circ$ , which is tracked well by both inviscid and viscous full-model solutions, while the inviscid forebody alone data shows no change in slope. This increase in normal force may be due to increased pressures on the aftbody at high angles of attack. Again, values of  $C_N$  are quite small for all angles of attack and have very small contributions towards lift, drag, and pitching moment characteristics.

Figure 7(c) shows very little difference in pitching moment characteristics between forebody and

full-model inviscid solutions. All computational predictions for  $C_m$  agree well with experimental data over the entire angle of attack range. Drag predictions (Fig. 7(e)) are similar to those for axial force, while lift coefficient and lift-to-drag ratio data are predicted well by the computational data for the full body. Based on the agreement between inviscid and viscous solutions for the wind tunnel configuration and their agreement with experimental data, it appears that viscous effect do not make a first order contribution to the aerodynamic characteristics of this configuration.

The level and nature of agreement between computational and experimental data is similar for other Mach numbers and configurations. The reader is again referred to References 7 and 8 for further comparison of computational and experimental results.

### Configuration Effects

One of the stated objectives of this test program was to provide aerodynamic data for three asymmetric tab/shelf configurations to allow vehicle designers to assess their feasibility for meeting mission requirements. The aerodynamic performance of these configurations is only one of many areas where trade studies will be performed to optimize vehicle mission performance. Thus, it is outside the scope of this work to make final determinations on the "goodness" or feasibility of one configuration versus another.

Figures 8(a)-8(f) present comparisons of longitudinal data for all four configurations tested: the baseline, the Ames, the canted tab, and the shelf. The axial force characteristics (Fig. 8(a)) remain essentially the same in trend, but with a positive increment that scales proportionally with projected control surface area (see Table 2). The normal force characteristic (Fig. 8(b)) for the three asymmetric configurations can also be viewed as incrementally different from the baseline values. The Ames configuration has the largest area of the three control surfaces and thus shows the largest negative increment in normal force. Normal force increments for all configurations are quite small in magnitude and vary only slightly with angle of attack.

Pitching moment characteristics for all four configurations are shown in Fig. 8(c). As stated previously, the goal for these fixed control surfaces is to allow the configuration to trim at a non-zero angle of attack in order to attain sufficient  $L/D$  values to satisfy mission requirements. All surfaces do show a shift in trim angle of attack, which again shows correlation to control surface area. The canted tab provides an  $11^\circ$  shift in trim angle, the shelf shows a  $13^\circ$  shift in trim angle, and the Ames tab shows a  $16^\circ$  shift in trim angle. All asymmetric configurations show a nearly constant positive increment in pitching moment, maintaining similar stability levels for all configurations. It is important to note that the pitching moment data presented herein are reduced about a non-realistic center of gravity location, namely the vehicle nose. When transferred to a realistic (further aft) position, the trim angle increments would become even larger and the asymmetric configurations would show a

lesser level of stability for all angles of attack. For example, Prabhu<sup>7</sup> presents both measured data and inviscid CFD pitching moment results reduced about a reference point at full-scale axial station -0.8659m (with no radial offset). This aft center of gravity location was derived from initial performance and packaging estimates. The Ames surface yields a trim point at  $\alpha \approx 17^\circ$ , the Canted tab yields a trim point at  $\alpha \approx 13^\circ$ , and the Shelf yields a trim point at  $\alpha \approx 14^\circ$  for this aft c.g. location. The corresponding L/D values for these trim points would meet or exceed stated performance metrics.

Corresponding to normal and axial force,  $C_L$  and  $C_D$  (Figs. 8(d) and 8(e)) show well-behaved increments over the angle of attack range. Fig. 8(f) shows that L/D varies only slightly among the one symmetric and three asymmetric configurations and that the trim angle to obtain L/D values in the 0.22 to 0.25 range are nominally 13 to 16 degrees. With a realistic aft c.g. placement, these data have shown this to be an attainable trim angle range for all control surfaces.

For completeness, Figs. 9, 10, and 11 show comparison of the four configurations at Mach 2.7, 3.5, and 4.5. No experimental data were obtained for the Ames configuration at  $M=4.5$ . As Mach number effects were shown to be small, the discussion of data trends at  $M=2.3$  are generally applicable to the higher Mach number data. As Mach number increases  $C_A$  and  $C_D$  curves tend to be generally smoother, while  $C_N$ ,  $C_m$ , and L/D tend to be more linear.

### **Concluding Remarks**

A 0.0376-scale model of a proposed Mars '07 Smart Lander configuration was tested in Leg II of the Unitary Plan Wind Tunnel at the NASA Langley Research Center. The objectives of the testing were to establish the stability and control characteristics of the proposed baseline vehicle and to assess the aerodynamic feasibility of three fixed control surfaces. Over 140 runs were obtained on four configurations, the baseline, the Ames surface, the Canted tab, and the Shelf, over a Mach range of 2.3 to 4.5. Mach effects were shown to be small on vehicle aerodynamic characteristics. Inviscid and viscous CFD predictions for the wind tunnel configuration geometry at wind tunnel conditions agreed well with measured data. Based on results from 3 different shelf/tab configurations, a fixed control surface appears to be a feasible concept for meeting aerodynamic performance metrics necessary to satisfy mission requirements.

### **Acknowledgements**

The authors gratefully acknowledge the following persons/groups for their contributions to this work: Ramadas K. Prabhu, Paresh Parikh, Mary Kae Lockwood, Glen J. Bobskill, Richard Wheless, John

Micol, Scott Goodliff, and The staff at the UPWT tunnel.

### **References**

1. Lockwood, M.K., et al.: "Entry Configurations and Performance Comparisons for the Mars Smart Lander" AIAA 2002-4407, August 2002.
2. Lockwood, M.K., Powell R.W., Graves, C.A., and Carman, G.L.: "Entry System Design Considerations for Mars Landers," American Astronautical Society Paper No. 01-023, 24<sup>th</sup> AAS Guidance and Control Conference, January 31-February 4 2001, Breckenridge, CO.
3. Erickson, G.E.: "Overview of Selected Measurement Techniques for Aerodynamic Testing in the NASA Langley Unitary Plan Wind Tunnel," AIAA 2000-2396, June 2000.
4. Hemsch, M.J.: private communication, June 2002.
5. Peiro, J, Peraire, J., and Morgan K.: "FELISA System Reference Manual and Users Guide," NASA CP-3291, May 1995.
6. Frink, N.T., and Pirzadeh, S.Z.: "Tetrahedral Finite-Volume Solutions to the Navier-Stokes Equations on Complex Configurations," NASA TM-1998-208961, December 1998.
7. Prabhu, R.K.: "An Inviscid Computational Study of Three '07 Mars Lander Aeroshell Configurations Over a Mach Number Range of 2.3 to 4.5," NASA CR-2001-211266.
8. Bobskill, G.J, Parikh, P.C., Prabhu, R.K., Tyler, E.D.: "Aerodynamic Database Development for Mars Smart Lander Vehicle Configurations," AIAA 2002-4411, August 2002.
9. Blake, W.W.: "Experimental Aerodynamic Characteristics of the Viking Entry Vehicle over the Mach Range 1.5 -10.0," NASA TR-3720106, April 1971.



**Table 1. Reference Dimensions**

Dimension	Full-Scale	.0376-Scale
$S_{ref}$	138.9 ft <sup>2</sup>	28.274 in <sup>2</sup>
$L_{ref}$ (vehicle diameter)	13.3 ft	6 in
$Xc.g._{ref}$ (at nose)	0 ft	0 in
$Yc.g._{ref}$ (at nose)	0 ft	0 in
$Zc.g._{ref}$ (at nose)	0 ft	0 in

**Table 2. Control Surface Areas**

Dimension	Full-Scale	.0376-Scale
$S_{Ames}$	9.372 ft <sup>2</sup>	1.908 in <sup>2</sup>
$S_{Canted}$	5.659 ft <sup>2</sup>	1.152 in <sup>2</sup>
$S_{Shelf}$	7.628 ft <sup>2</sup>	1.553 in <sup>2</sup>

**Table 3. Balance Uncertainties for LaRC 2008**

		NF(lbs)	AF(lbs)	PM(in-lbs)	RM(in-lbs)	YM(in-lbs)	SF(lbs)
Maximum Load		60	180	150	30	120	60
Accuracy (%full-scale)		0.1	0.32	0.11	0.27	0.15	0.05
Accuracy (Load)		0.06	0.576	0.165	0.081	0.18	0.03
Mach	$q_{\infty}$ (psi)	CN $\pm 2\sigma$	CA $\pm 2\sigma$	CM $\pm 2\sigma$	CRM $\pm 2\sigma$	CYM $\pm 2\sigma$	CY $\pm 2\sigma$
		Accuracy	Accuracy	Accuracy	Accuracy	Accuracy	Accuracy
2.3	2.972	$\pm 0.00071$	$\pm 0.00686$	$\pm 0.00033$	$\pm 0.00016$	$\pm 0.00036$	$\pm 0.00036$
2.7	2.704	$\pm 0.00078$	$\pm 0.00753$	$\pm 0.00036$	$\pm 0.00018$	$\pm 0.00039$	$\pm 0.00039$
3.5	2.110	$\pm 0.00101$	$\pm 0.00965$	$\pm 0.00046$	$\pm 0.00023$	$\pm 0.00050$	$\pm 0.00050$
4.5	1.587	$\pm 0.00134$	$\pm 0.01284$	$\pm 0.00061$	$\pm 0.00030$	$\pm 0.00067$	$\pm 0.00067$

**Table 4. UPWT Test Matrix for Mars '07 Smart Lander Test 1735**

Configuration	Re/ft $\times 10^6$	Grit	$\alpha$	$\beta$	Mach 2.3	Mach 2.7	Mach 3.5	Mach 4.5
Baseline	2.0	None	A1 <sup>1</sup>	0	Run 59	Run 64	Run 69	Run 76
Baseline	2.0	None	A2 <sup>2</sup>	2	Run 60	Run 65	Run 70	Run 77
Baseline	2.0	None	A2	4	Run 61	Run 66	Run 71	Run 78
Baseline	2.0	None	A3 <sup>3</sup>	B1 <sup>4</sup>	Run 149	Run 151	-	-
Ames	2.0	None	A1	0	Run 81	Run 84	Run 88	-
Ames	2.0	None	A2	2	Run 82	Run 85	Run 89	-
Ames	2.0	None	A2	4	Run 83	Run 86	Run 90	-
Ames	2.0	None	A3	B1	-	-	-	-
Shelf	2.0	None	A1	0	Run 93	Run 99	Run 103	Run 114
Shelf	2.0	None	A2	2	Run 94	Run 100	Run 105	Run 116
Shelf	2.0	None	A2	4	Run 95	Run 101	Run 106	Run 117
Shelf	2.0	None	A3	B1	Run 96	Run 102	Run 107	Run 115
Canted	2.0	None	A1	0	Run 119	Run 123	Run 128	Run 134
Canted	2.0	None	A2	2	Run 120	Run 124	Run 129	Run 135
Canted	2.0	None	A2	4	Run 121	Run 125	Run 130	Run 136
Canted	2.0	None	A3	B1	Run 122	Run 126	Run 131	Run 138

<sup>1</sup>A1: Alpha -5,-4,-3,-2,-1,0,1,2,3,4,5,6,7,8,9,10,11,12,13,14,15,16,17,18,19,20<sup>2</sup>A2: Alpha -5,-2,0,2,4,6,8,10,11,12,13,14,16,18,20<sup>3</sup>A3: Trim Angle of Attack for each configuration<sup>4</sup>B1: Beta -5,-4,-3,-2,-1,0,1,2,3,4,5

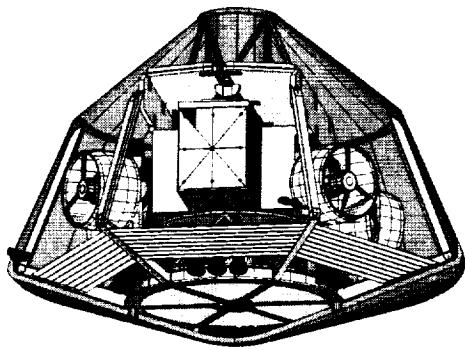


**Figure 1.** Schematic of Proposed Mars '07 Lander Configuration

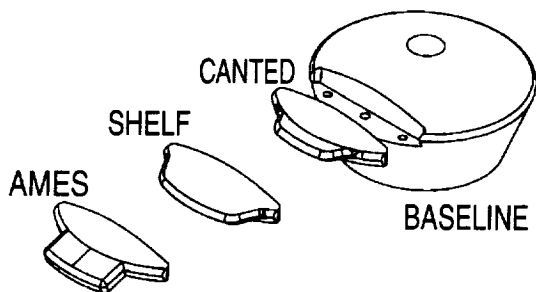


**Figure 2.** Schematic of Proposed Control Surfaces for Smart Lander

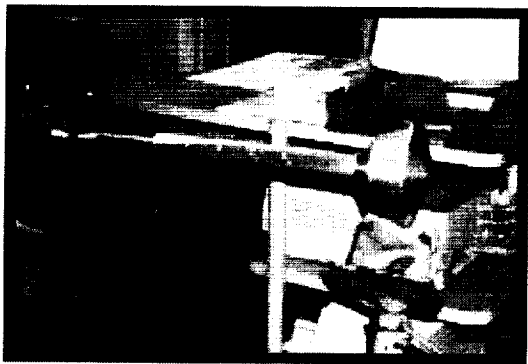


**Figure 3.** Photograph of Wind Tunnel Model with Balance Shroud



**Figure 4(a).** Installation of Mars Smart Lander Baseline Model in the UPWT at LaRC.

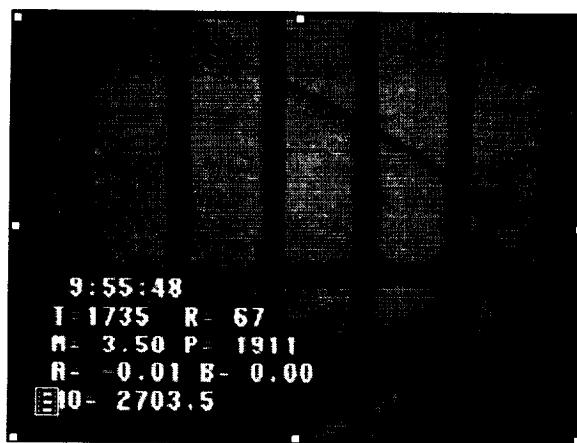


**Figure 4(b).** Schlieren Photograph of Mars Smart Lander Model in the UPWT at LaRC

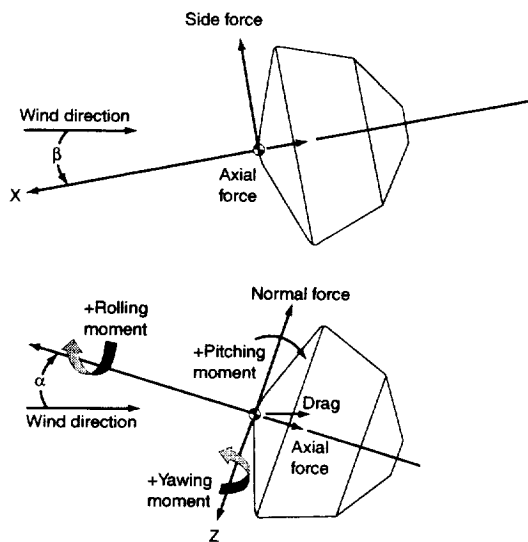


**Figure 5.** Aerodynamic Coordinate System.

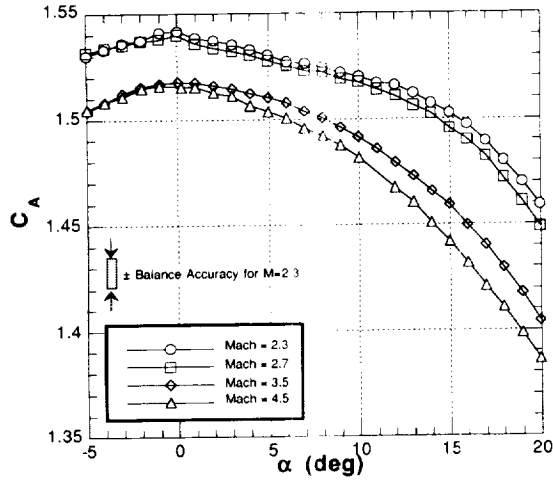


**Figure 6(a).** Effect of Mach Number on Measured Axial Force Coefficient for Baseline Configuration

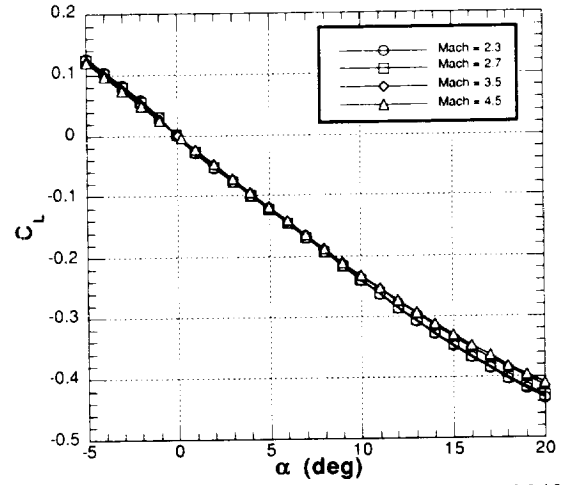


**Figure 6(d).** Effect of Mach Number on Measured Lift Force Coefficient for Baseline Configuration

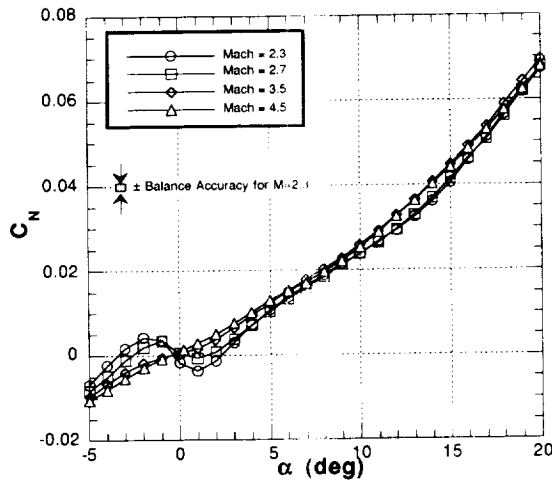


**Figure 6(b).** Effect of Mach Number on Measured Normal Force Coefficient for Baseline Configuration

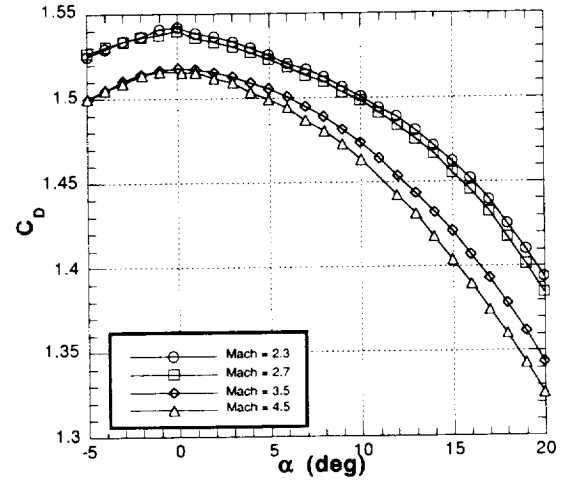


**Figure 6(e).** Effect of Mach Number on Measured Drag Force Coefficient for Baseline Configuration

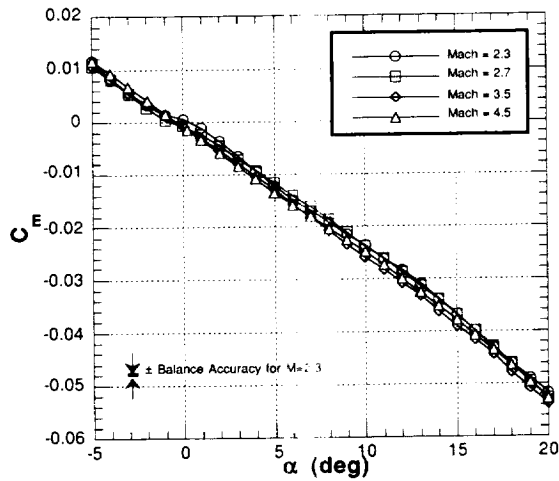


**Figure 6(c).** Effect of Mach Number on Measured Pitching Moment Coefficient for Baseline Configuration

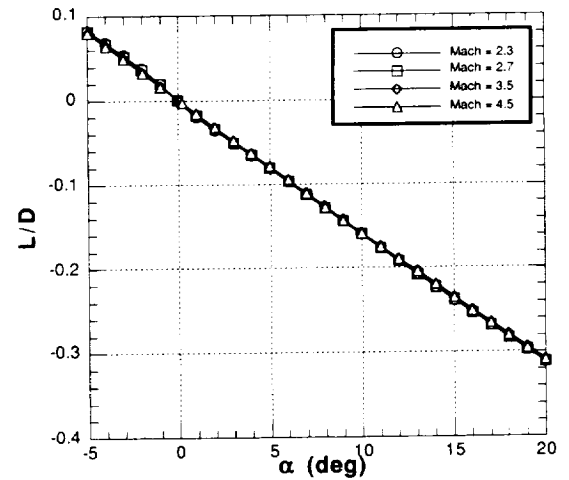


**Figure 6(f).** Effect of Mach Number on Measured Lift-to-Drag Ratio for Baseline Configuration

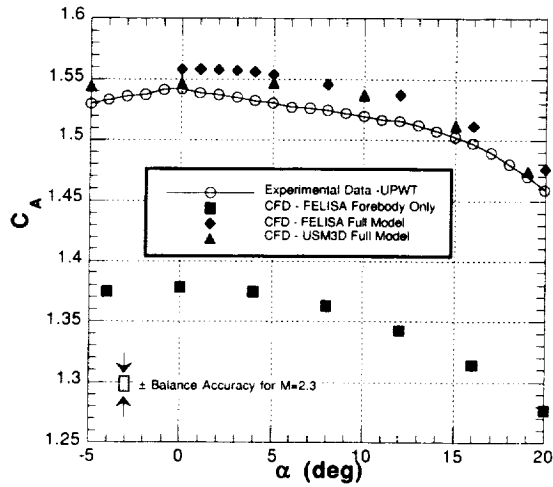


**Figure 7(a).** Comparison of Measured and Predicted Axial Force Coefficient for Baseline Configuration at Mach 2.3

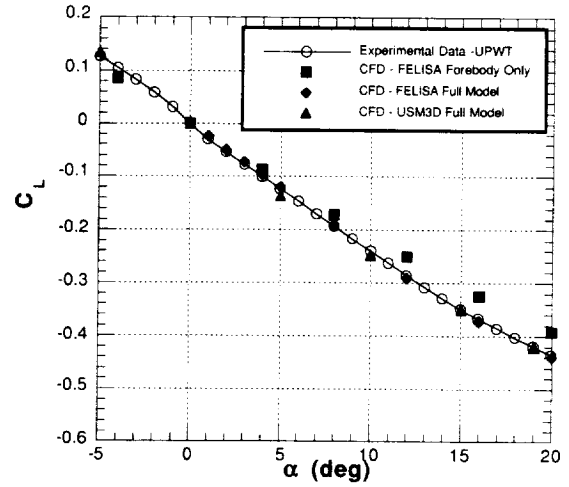


**Figure 7(d).** Comparison of Measured and Predicted Lift Force Coefficient for Baseline Configuration at Mach 2.3

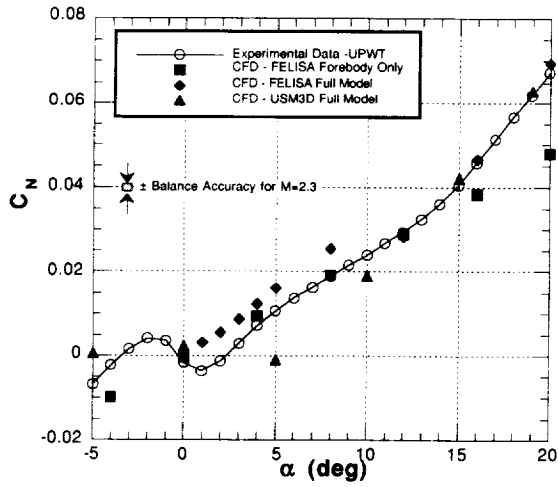


**Figure 7(b).** Comparison of Measured and Predicted Normal Force Coefficient for Baseline Configuration at Mach 2.3

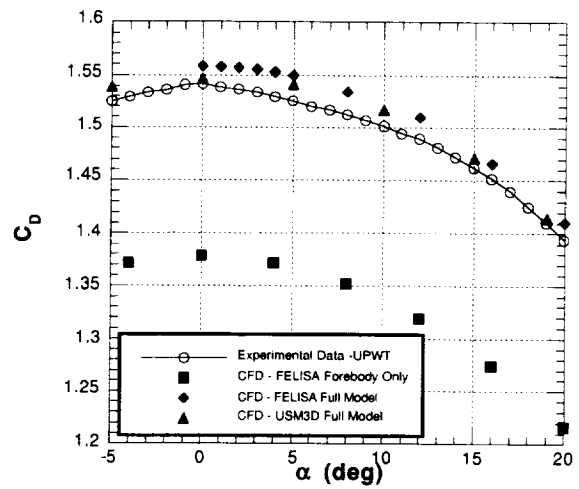


**Figure 7(e).** Comparison of Measured and Predicted Drag Force Coefficient for Baseline Configuration at Mach 2.3

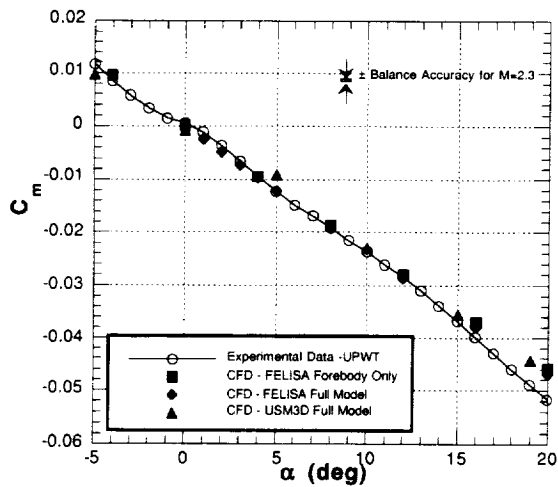


**Figure 7(c).** Comparison of Measured and Predicted Pitching Moment Coefficient for Baseline Configuration at Mach 2.3

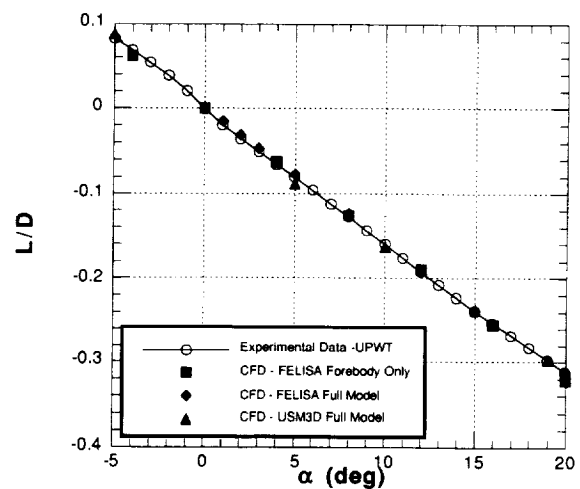


**Figure 7(f).** Comparison of Measured and Predicted Lift-to-Drag Ratio for Baseline Configuration at Mach 2.3

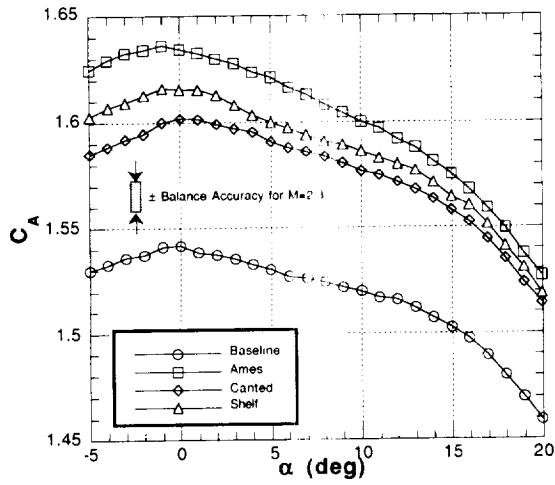


**Figure 8(a).** Effect of Fixed Control Surface on Measured Axial Force Coefficient at Mach 2.3

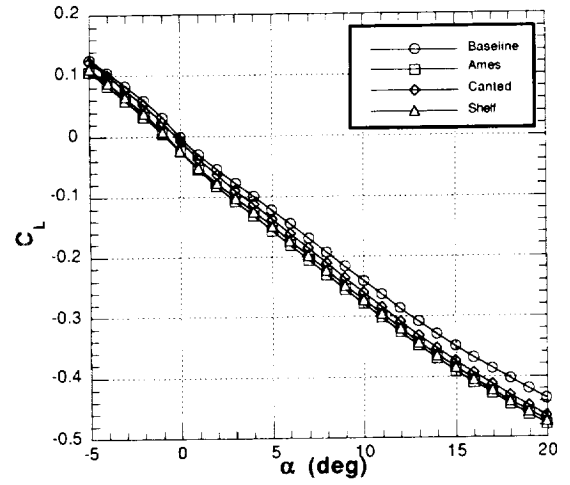


**Figure 8(d).** Effect of Fixed Control Surface on Measured Lift Force Coefficient at Mach 2.3

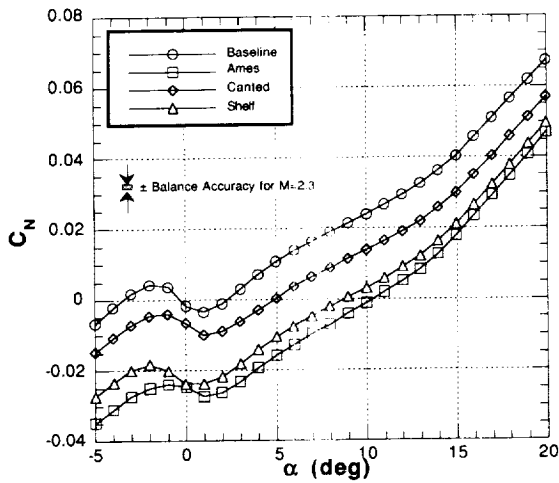


**Figure 8(b).** Effect of Fixed Control Surface on Measured Normal Force Coefficient at Mach 2.3

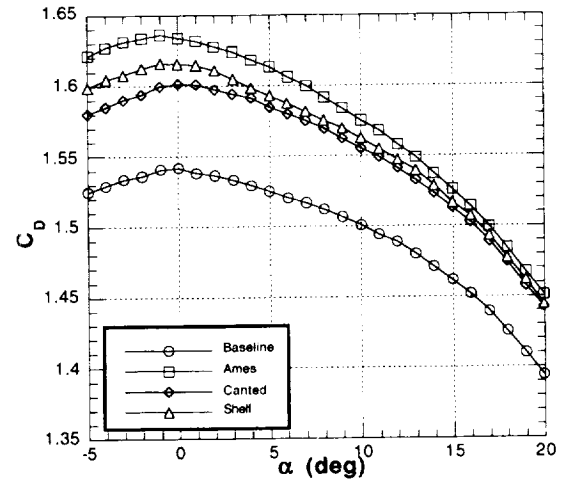


**Figure 8(e).** Effect of Fixed Control Surface on Measured Drag Force Coefficient at Mach 2.3

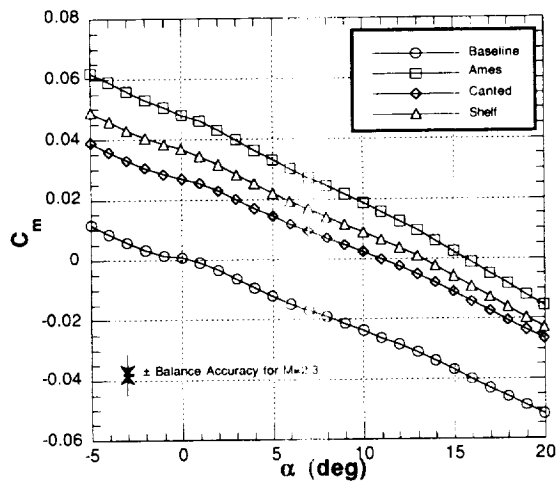


**Figure 8(c).** Effect of Fixed Control Surface on Measured Pitching Moment Coefficient at Mach 2.3

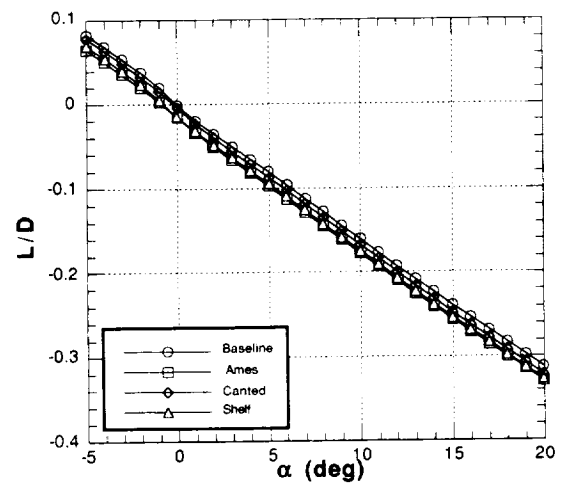


**Figure 8(f).** Effect of Fixed Control Surface on Measured Lift-to-Drag Ratio at Mach 2.3

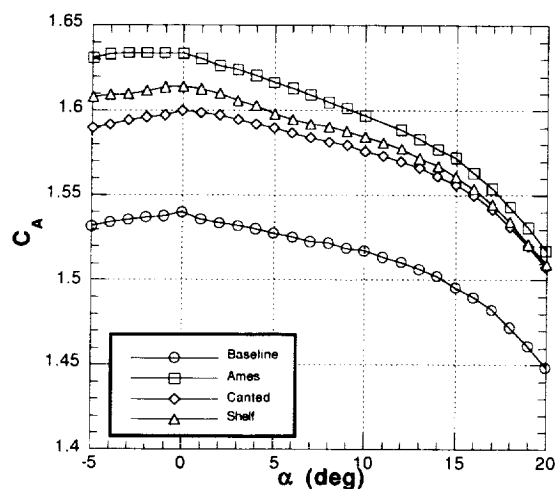


**Figure 9(a).** Effect of Fixed Control Surface on Measured Axial Force Coefficient at Mach 2.7

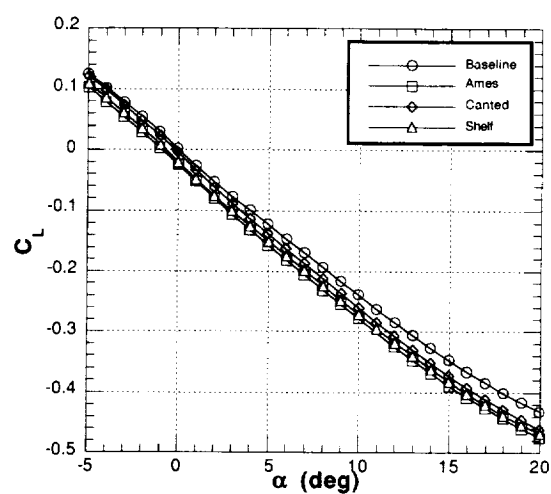


**Figure 9(d).** Effect of Fixed Control Surface on Measured Lift Force Coefficient at Mach 2.7

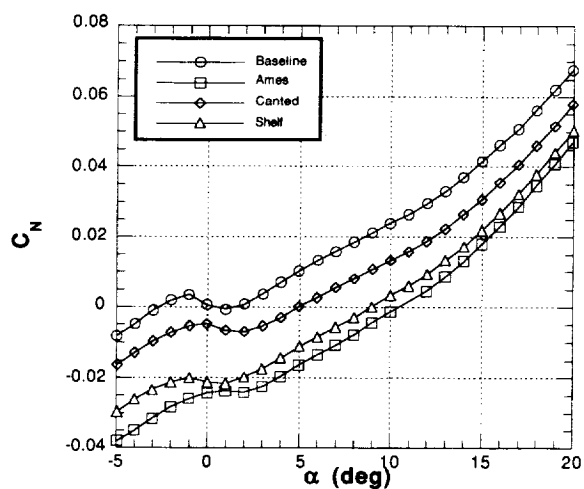


**Figure 9(b).** Effect of Fixed Control Surface on Measured Normal Force Coefficient at Mach 2.7

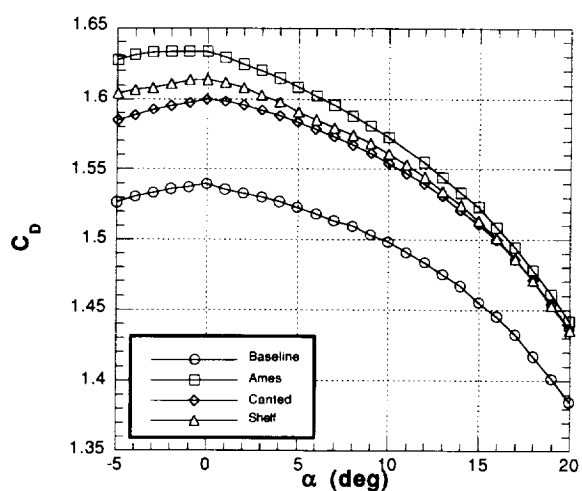


**Figure 9(e).** Effect of Fixed Control Surface on Measured Drag Force Coefficient at Mach 2.7

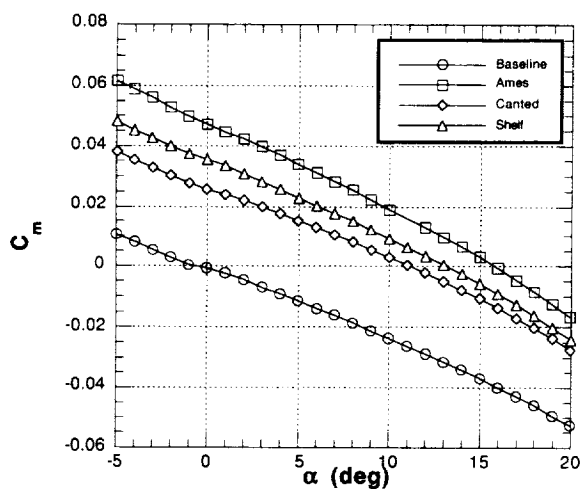


**Figure 9(c).** Effect of Fixed Control Surface on Measured Pitching Moment Coefficient at Mach 2.7

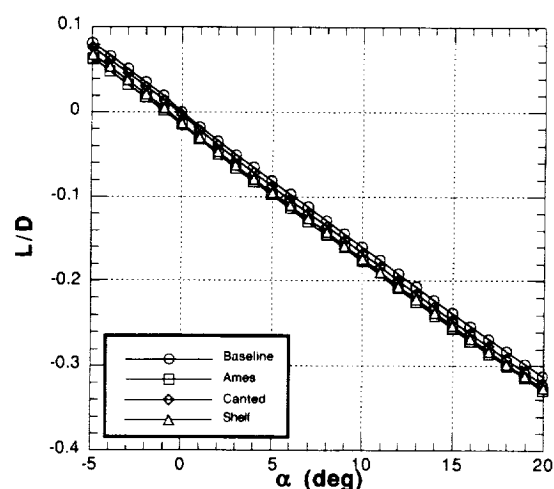


**Figure 9(f).** Effect of Fixed Control Surface on Measured Lift-to-Drag Ratio at Mach 2.7

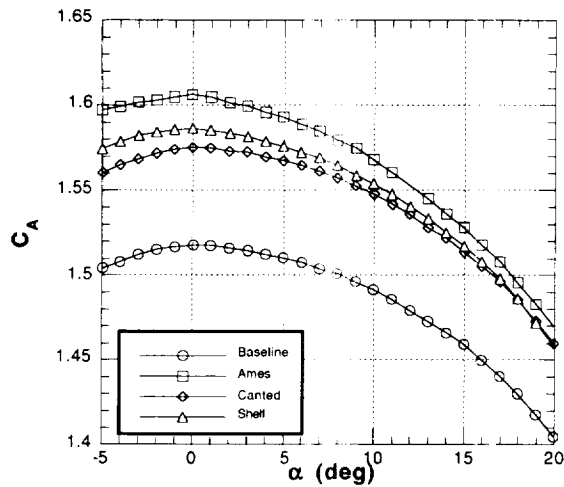


**Figure 10(a).** Effect of Fixed Control Surface on Measured Axial Force Coefficient at Mach 3.5

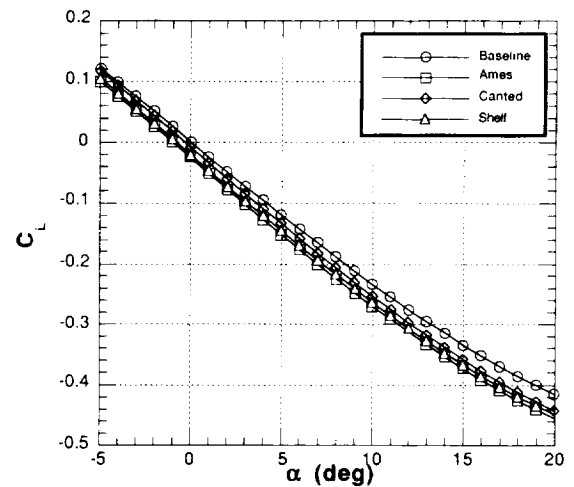


**Figure 10(d).** Effect of Fixed Control Surface on Measured Lift Force Coefficient at Mach 3.5

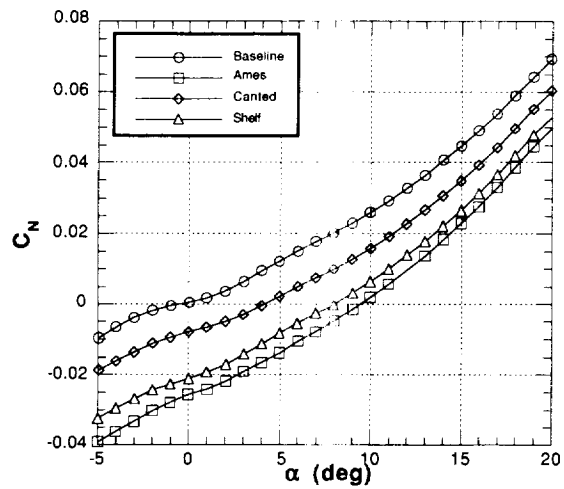


**Figure 10(b).** Effect of Fixed Control Surface on Measured Normal Force Coefficient at Mach 3.5

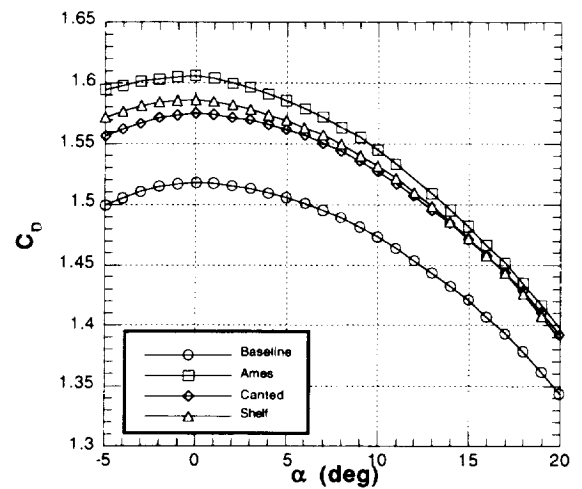


**Figure 10(e).** Effect of Fixed Control Surface on Measured Drag Force Coefficient at Mach 3.5

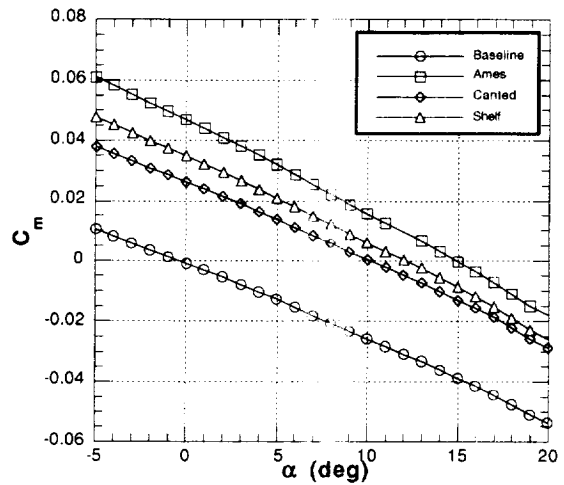


**Figure 10(c).** Effect of Fixed Control Surface on Measured Pitching Moment Coefficient at Mach 3.5

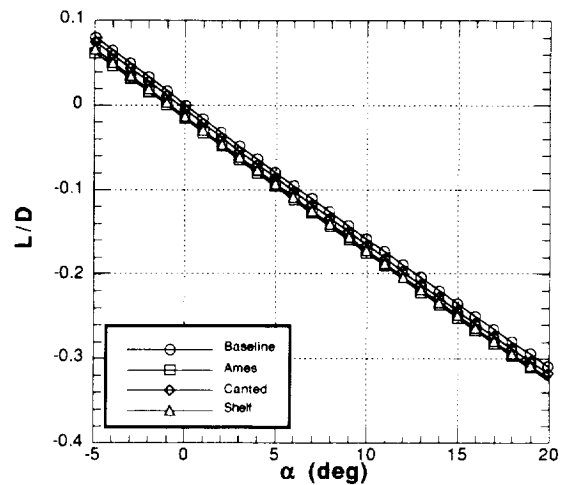


**Figure 10(f).** Effect of Fixed Control Surface on Measured Lift-to-Drag Ratio at Mach 3.5

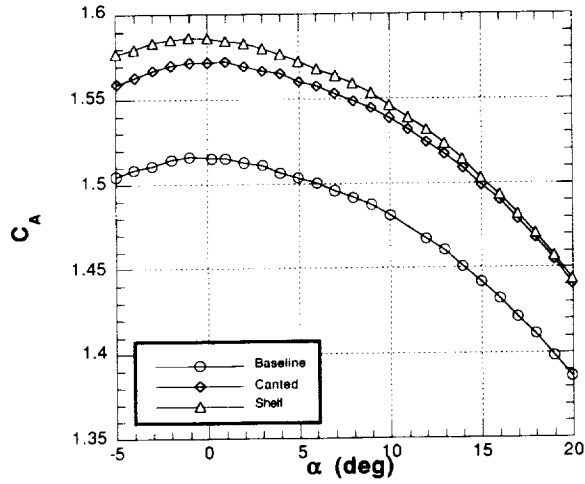


**Figure 11(a).** Effect of Fixed Control Surface on Measured Axial Force Coefficient at Mach 4.5

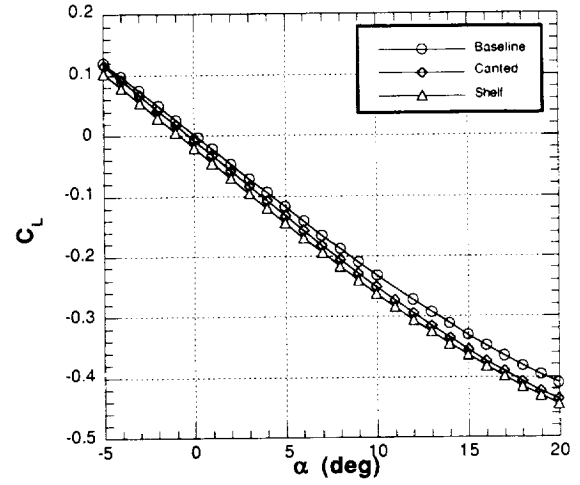


**Figure 11(d).** Effect of Fixed Control Surface on Measured Lift Force Coefficient at Mach 4.5

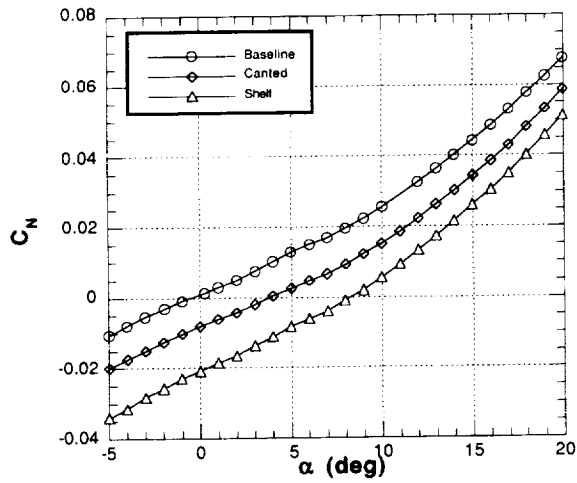


**Figure 11(b).** Effect of Fixed Control Surface on Measured Normal Force Coefficient at Mach 4.5

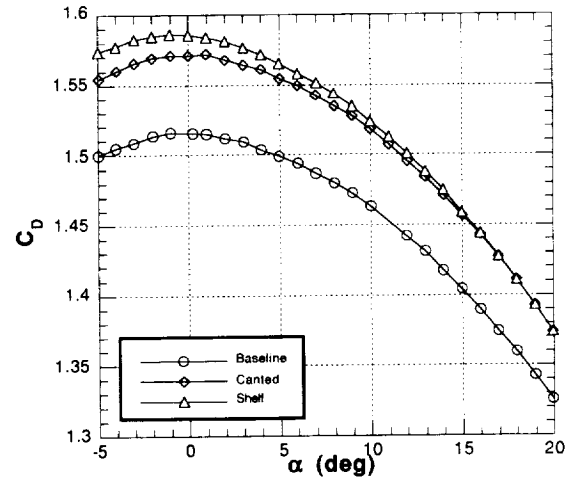


**Figure 11(e).** Effect of Fixed Control Surface on Measured Drag Force Coefficient at Mach 4.5

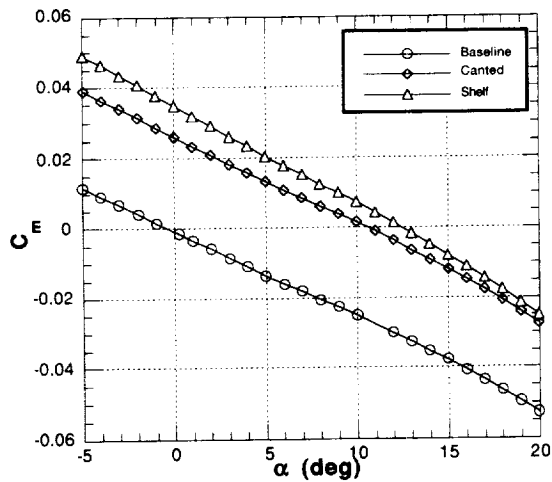


**Figure 11(c).** Effect of Fixed Control Surface on Measured Pitching Moment Coefficient at Mach 4.5

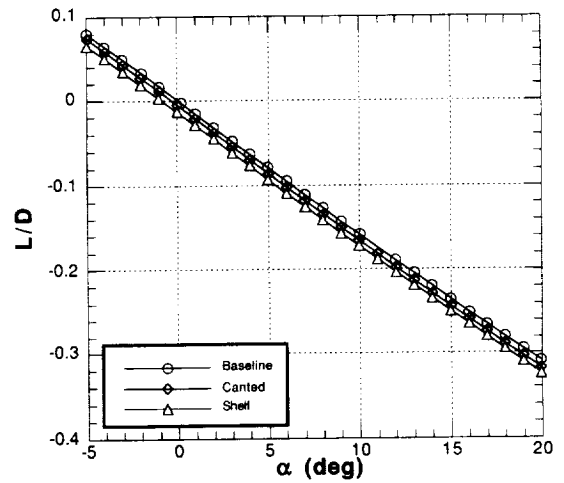


**Figure 11(f).** Effect of Fixed Control Surface on Measured Lift-to-Drag Ratio at Mach 4.5